ACS NANO

Open Access

This article is licensed under CC-BY-NC-ND 4.0

www.acsnano.org

ARTICLE

# Defect Engineering of $MoTe_2$ via Thiol Treatment for Type III van der Waals Heterojunction Phototransistor

Yeonsu Jeong, Bin Han, Adrián Tamayo, Nathalie Claes, Sara Bals, and Paolo Samorì*

Cite This: *ACS Nano* 2024, 18, 18334−18343

Read Online

ACCESS | Metrics & More | Article Recommendations | Supporting Information

**ABSTRACT:** **Molybdenum ditelluride ($MoTe_2$) nanosheets have displayed intriguing physicochemical properties and opto-electric characteristics as a result of their tunable and small band gap ($E_g$ ~ 1 eV), facilitating concurrent electron and hole transport. Despite the numerous efforts devoted to the development of p-type $MoTe_2$ field-effect transistors (FETs), the presence of tellurium (Te) point vacancies has caused serious reliability issues. Here, we overcome this major limitation by treating the $MoTe_2$ surface with thiolated molecules to heal Te vacancies. Comprehensive materials and electrical characterizations provided unambiguous evidence for the efficient chemisorption of butanethiol. Our thiol-treated $MoTe_2$ FET exhibited a 10-fold increase in hole current and a positive threshold voltage shift of 25 V, indicative of efficient hole carrier doping. We demonstrated that our powerful molecular engineering strategy can be extended to the controlled formation of van der Waals heterostructures by developing an n-$SnS_2$/thiol-$MoTe_2$ junction FET (thiol-JFET). Notably, the thiol-JFET exhibited a significant negative photoresponse with a responsivity of 50 A $W^{-1}$ and a fast response time of 80 ms based on band-to-band tunneling. More interestingly, the thiol-JFET displayed a gate tunable trimodal photodetection comprising two photoactive modes (positive and negative photoresponse) and one photoinactive mode. These findings underscore the potential of molecular engineering approaches in enhancing the performance and functionality of $MoTe_2$-based nanodevices as key components in advanced 2D-based optoelectronics.**

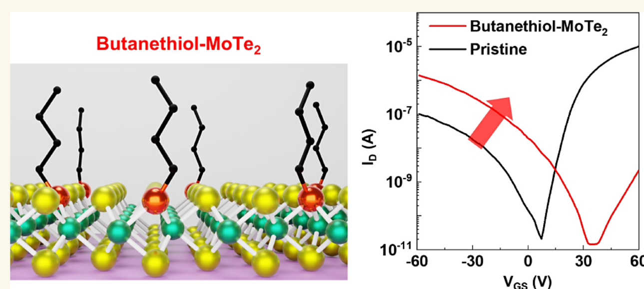


**KEYWORDS:** *vacancy healing, thiol treatment, van der Waals heterojunction, negative photoresponse, $SnS_2$/$MoTe_2$*

Downloaded via UNIV OF ANTWERPEN on July 30, 2024 at 10:37:54 (UTC).
See https://pubs.acs.org/sharingguidelines for options on how to legitimately share published articles.

During the past decade, two-dimensional (2D) transition metal dichalcogenides (TMDs) have attracted tremendous interest because of their intriguing and diverse physicochemical and opto-electrical properties.[1−4] Among the various TMDs, molybdenum ditelluride ($MoTe_2$) has emerged as a next-generation semiconductor with a bandgap of approximately 1 eV, being comparable to that of silicon.[5] Consequently, a range of optoelectronic devices exploiting $MoTe_2$ as an active material such as PN diodes, field-effect transistors (FETs), and heterojunction transistors, have been reported.[6−10] However, $MoTe_2$-based devices still suffer from serious reliability issues associated with the majority carrier polarity, irrespective of contact metals.[11−13] This reliability concern primarily stems from tellurium (Te) point vacancies in $MoTe_2$, which are its predominant structural defects as revealed by scanning transmission electron microscopy and density functional theory calculations.[14,15] Te vacancies introduce midgap defect states near the conduction band, leading to strong electron polarities or ambipolar properties in $MoTe_2$ devices.[13,14]

Endeavors to achieve high performance stable p-type $MoTe_2$ FETs have been ongoing, by employing numerous methods, such as physisorption of oxygen containing molecules and surface charge transfer using functional polymers and $MoO_3$ oxide.[16−22] For example, Chang et al. achieved reversible p/n-type doping of $MoTe_2$ transistors by physisorbing $O_2$ or $H_2O$ on the air-sensitive $MoTe_2$ channel surface.[16] In another report, Ke et al. demonstrated p-doping of $MoTe_2$ FETs through damage-free laser irradiation on multilayer $MoTe_2$ in a

Received: February 16, 2024
Revised: May 12, 2024
Accepted: May 22, 2024
Published: July 3, 2024

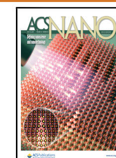



© 2024 The Authors. Published by American Chemical Society

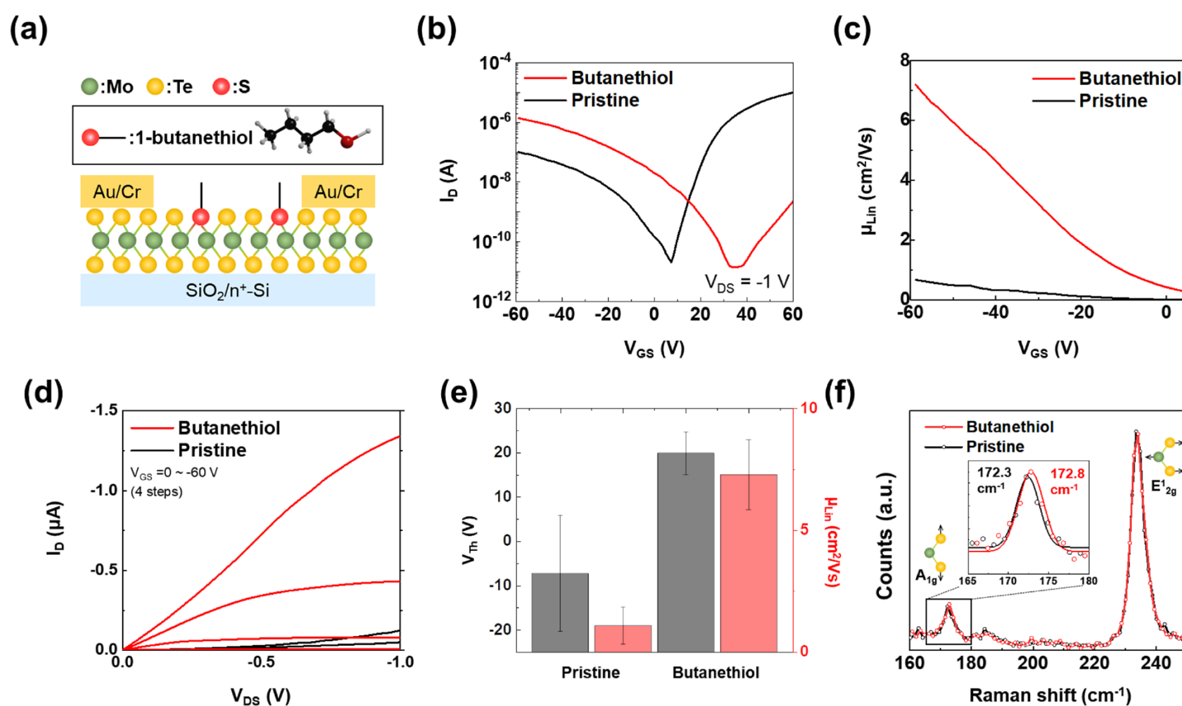


**Figure 1. Electrical and Raman characterization of thiol-$MoTe_2$FET. (a) Cross-section schematics of a thiol-$MoTe_2$ FET whose Te vacancies are healed by 1-butanethiol. (b) Transfer characteristics, (c) linear mobility ($\mu_{Lin}$) plots, and (d) output characteristics of the ambipolar pristine $MoTe_2$ in black and p-type thiol-$MoTe_2$ FET in red. (e) The average threshold voltage ($V_{Th}$) and $\mu_{Lin}$ of 14 different $MoTe_2$ FETs before and after the butanethiol surface treatment to ensure its reproducibility. All error bars represent the standard deviation from independent measurements ($n$ = 14). Relative standard deviation values for $V_{Th}$ and mobility in pristine devices are estimated to be ±13.1 and ±0.7, respectively, while those after butanethiol surface treatment are ±5.7 and ±1.4. (f) Raman spectra of pristine $MoTe_2$ and thiol-$MoTe_2$, along with the enlarged inset graph from 165 to 180 $cm^{-1}$ showing a blue shift of $A_{1g}$.**

localized channel area.[17] However, these devices still retain air-vulnerable defective $MoTe_2$ surfaces, leading to significant shifts in threshold voltage ($V_{Th}$) under vacuum conditions due to the easy removal of molecules physisorbed on the $MoTe_2$ channel surface. More recently, Cho et al. utilized a 10 nm-thin $MoO_3$/PDMS polymer layer to withdraw electrons from multilayer $MoTe_2$, enhancing hole carrier concentrations in p-$MoTe_2$ FETs by up to an order of magnitude.[19] Similar charge transfer-based effective p-doping on monolayer $MoTe_2$ also has been introduced using polymer encapsulation and superacid doping with PMMA and TFSI.[20] However, these surface charge transfer p-doping methods on $MoTe_2$ flakes have primarily been applied to single-channel devices rather than a heterostacked channel. In other words, despite the improved electrical performances of p-$MoTe_2$ in terms of hole carrier concentrations, several unresolved issues persist, including limited device operations under inert conditions and lack of applicability due to thick polymer layers coating the $MoTe_2$ nanosheets.[18−20] Moreover, beyond single-channel $MoTe_2$ device, further extended devices or practical applications have rarely been reported, although it would be equally important to fully exploit the p-type semiconducting properties in complex heterojunction systems.[6,23]

A junction field-effect transistor (JFET) comprising tin disulfide ($SnS_2$) and $MoTe_2$ was theoretically proposed by Szabo et al. in 2015, leveraging the band-to-band tunneling (BTBT) phenomenon.[24] $SnS_2$, with a substantial electron affinity around 5.2 eV, maintains an n-type polarity, which is critical for forming type III band alignment with many other p-type TMD materials, which may be of interest for next generation tunneling FETs.[25,26] While a $MoTe_2$/$SnS_2$ JFET was successfully fabricated by Kim et al. in 2020, the device exhibited only strong electron polarities.[27] To address this challenge, Chen et al. achieved control over the charge polarity of the $MoTe_2$/$SnS_2$ JFET through the surface adsorption of oxygen containing molecules.[28] However, the weak physical interaction between oxygen and $MoTe_2$ can result in unstable operation in ambient air.[28,29] Although the above discussion underscores the growing interest in reliable p-doping methods for $MoTe_2$ and its practical applications, reports on BTBT in p-$MoTe_2$/n-$SnS_2$ type III heterojunctions remain scarce due to the low hole concentration in $MoTe_2$. Developing a robust and effective p-type doping method for $MoTe_2$ is expected to provide an additional p-type TMD material, complementing the existing research focused on $WSe_2$-based type III heterojunction studies.[30,31]

In the present work, we successfully introduced a molecular engineering strategy to enhance p-type polarities of $MoTe_2$. Butanethiol treatment of $MoTe_2$ FET caused a positive $V_{Th}$ shift of ca. 25 V, indicating a reduction in midgap defect states near the conduction band. This effect can be unambiguously ascribed to the effective healing of Te vacancies via butanethiol chemisorption. While the viability of thiol-based defect healing of chalcogen vacancies has been previously reported for 2D TMDs such as $MoS_2$, $WS_2$, and $WSe_2$,[2,22,32] the healing of Te vacancies in $MoTe_2$ and other ditellurides has not yet been demonstrated. In addition, reliable device operation of butanethiol-treated $MoTe_2$ (thiol-$MoTe_2$) FET under different conditions − $N_2$, air, and ultrahigh vacuum (UHV) − validated the formation of Mo−S bonds on the $MoTe_2$ basal plane. Raman spectroscopy and X-ray photoelectron spectroscopy (XPS) analyses further revealed the p-doping effect in thiol-


https://doi.org/10.1021/acsnano.4c02207
ACS Nano 2024, 18, 18334−18343

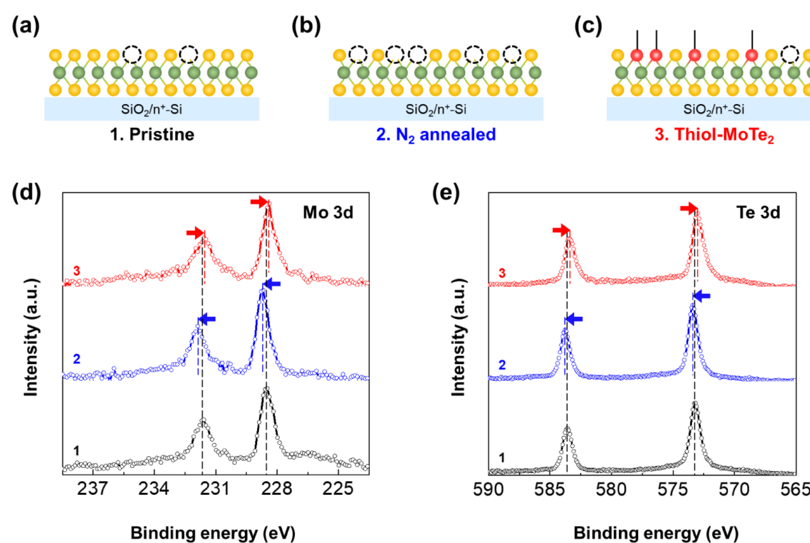


**Figure 2. High-resolution XPS analysis of surface functionalized $MoTe_2$. (a−c) 2D schematics of $MoTe_2$ under different conditions: (1) pristine (black), (2) after hot plate annealing at 250 °C for 2 h in $N_2$ (blue), and (3) after butanethiol treatment (red). Dark circles denote Te vacancies of $MoTe_2$; red spheres represent the sulfur atoms of butanethiols. (d, e) High-resolution XPS Mo 3d and Te 3d core-level spectra of thiol-$MoTe_2$ (red) compared to the corresponding pristine (black) and Te vacancy-induced surface (blue). XPS analyses were conducted primarily to investigate the surface binding states of $MoTe_2$ under different three conditions, as shown in a−c.**

$MoTe_2$. Moreover, we extended our molecular engineering approach to the fabrication of a JFET comprising thiol-$MoTe_2$ and n-$SnS_2$. By taking advantage of the high hole concentration in thiol-$MoTe_2$, the JFET demonstrated excellent antiambipolar transfer characteristics with an $I_{ON}/I_{OFF}$ ratio of $10^2$. Notably, our JFET exhibited a significant negative photoresponse (NPR) with a responsivity ($R$) of 50 A $W^{-1}$ and fast response time of 80 ms based on BTBT. This work demonstrates the possibility to achieve NPR due to BTBT using a $MoTe_2$-based JFET. Additionally, our powerful approach enabled us to achieve enhanced optoelectrical characteristics, including a 20-fold increased positive photoresponsivity, and a ca. 5 times faster photoresponse time compared to the control sample. Intriguingly, we observed a falling time of NPR at 455 nm photoswitching being ~3 times faster than the rising time, a behavior not detected in conventional 2D TMD-based photodetectors due to slow charge trap/detrapping in midgap defect states. Overall, the controlled molecular functionalization of the $MoTe_2$ surface made it possible to develop reliable and high-performance p-type FETs and JFET photodetectors.

## RESULTS AND DISCUSSION

Figure 1a illustrates the cross-section of a thiol-$MoTe_2$ FET, highlighting the healed Te vacancies on the $MoTe_2$ channel through a 1-butanethiol surface treatment. All devices in this study are bottom gate, supported on 270 nm $SiO_2/n^+$-Si coated with Au/Cr (50 nm/3 nm) patterns serving as the source/drain (S/D) electrodes. Atomic force microscopy (AFM) topographical imaging confirmed that pristine $MoTe_2$ flakes are 5 nm thick, as shown in Figure S1. Upon butanethiol treatment, the thickness remained similar, without evidence of the formation of a thick adlayer on top of the $MoTe_2$ flake. Meanwhile, the surface roughness of exfoliated flakes decreased from 0.65 to 0.33 nm, as shown in Figure S2. Figure 1b compares the transfer characteristic ($I_D-V_{GS}$) of the thiol-$MoTe_2$ in red vs the pristine $MoTe_2$ FET in black. Both electrical measurement and thiol-functionalization on $MoTe_2$ were conducted under $N_2$ atmosphere in the glovebox to eliminate possible hole doping effects caused by oxygen absorption.[13,16] The pristine $MoTe_2$ FET exhibited ambipolar characteristics, with its electron current being 2 orders of magnitude higher than the hole current. Upon butanethiol treatment, the hole current dramatically increased by approximately 1 order of magnitude at $V_{GS}$ = −60 V, while the electron current decreased by 4 orders of magnitude at $V_{GS}$ = 60 V. The $V_{Th}$ also showed a positive shift of ca. 25 V when considering $I_D = 10^{-9}$ A as the reference. The increased hole current and positive threshold shift consistently indicate efficient hole carrier doping upon butanethiol treatment. Figure 1c reveals that the thiol functionalization yields a 10-fold increase in the linear mobility ($\mu_{Lin}$), reaching ~7 $cm^2$ $V^{-1}$ $s^{-1}$. Additionally, the output characteristics ($I_D-V_{DS}$) of the two FETs in Figure 1d provide evidence for an ohmic-like behavior in both S/D contacts, yet the $I_D$ of the thiol-$MoTe_2$ FET is roughly 10 times higher. To verify the reproducibility of butanethiol surface treatment on $MoTe_2$, we fabricated 14 different thiol-$MoTe_2$ devices, observing an average positive $V_{Th}$ shift of approximately +25 V (Figure 1e). Moreover, we recorded an 8-fold increase in the average $\mu_{Lin}$, confirming the p-doping effect. Figure S3 displays the individual transistor transfer curves and corresponding mobility plots. Significantly, the thiol-$MoTe_2$ FET showed far more improved air-stable electrical performances compared with the pristine one (Figure S4). Under $V_{GS}$ = 0 V, the $I_D$ of thiol-$MoTe_2$ FET remained almost identical, while the control sample showed more than a 100-fold change in $I_D$ under different ambient conditions ($N_2$, air, and UHV ~ $10^{-5}$ Torr), after 5 h of exposure to each condition, with the hole current decreasing dramatically from 20 nA in air to 0.1 nA under UHV. Such result indicates that the Te vacancies, which render the device vulnerable to external environment, are healed effectively via thiol treatment. Raman spectroscopy further confirmed the p-type doping effect of butanethiol treatment on $MoTe_2$, inducing a blue-shift of the $A_{1g}$ peak from 172.3 to 172.8 $cm^{-1}$, as shown in Figure 1f.[20,21]


https://doi.org/10.1021/acsnano.4c02207
ACS Nano 2024, 18, 18334−18343

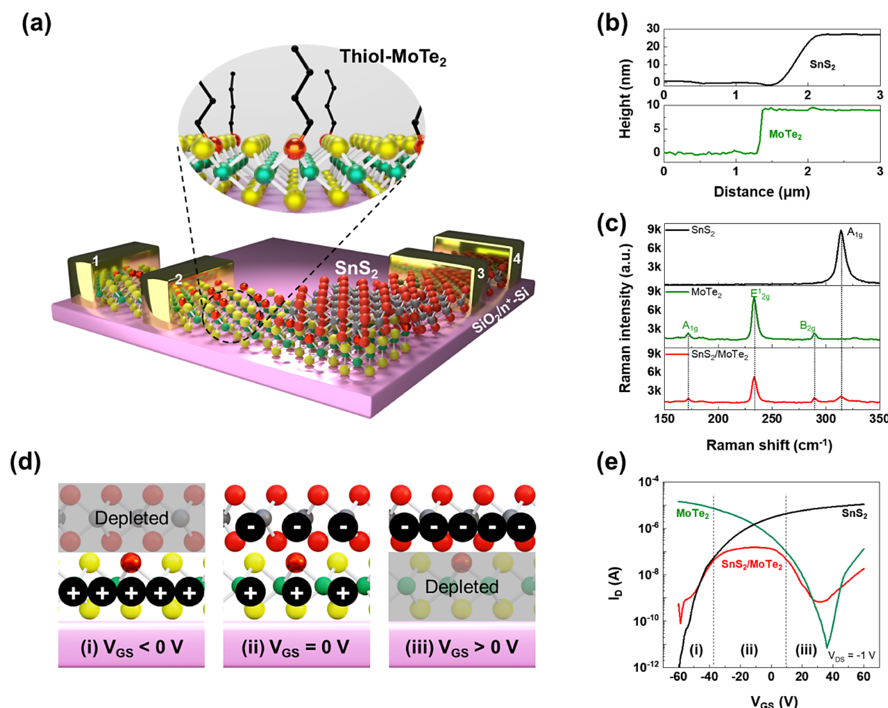


**Figure 3. Material characteristics and electrical performance of $SnS_2$/thiol-$MoTe_2$ JFET. (a) 3D schematic view of $SnS_2$/thiol-$MoTe_2$ heterojunction FET. The red spheres on the thiol-$MoTe_2$ represent where the Te vacancies are healed by the butanethiol. (b) Thickness profiles of $SnS_2$ (black) and thiol-$MoTe_2$ (green) as obtained from AFM. (c) Raman spectra of $SnS_2$, thiol-$MoTe_2$, and $SnS_2$/thiol-$MoTe_2$ junction area. $SnS_2$ shows the peak at 314.2 $cm^{-1}$ for $A_{1g}$ mode while thiol-$MoTe_2$ exhibits three peaks at 172.8 $cm^{-1}$, 234.0 $cm^{-1}$, and 289.5 $cm^{-1}$ for $A_{1g}$, $E^1_{2g}$ and $B_{2g}$, respectively. The Raman peak positions from $SnS_2$/thiol-$MoTe_2$ heterojunction exactly match those observed in corresponding individual flakes. (d) Magnified van der Waals heterojunction of our JFET, showing (i) OFF state with electron-depletion under $V_{GS} < 0$ V, (ii) ON under $V_{GS} = 0$ V, and (iii) OFF with hole-depletion under $V_{GS} > 0$ V. (e) Transfer characteristics of the thiol-$MoTe_2$ (green), $SnS_2$ (black), and $SnS_2$/thiol-$MoTe_2$ (red).**

In order to attain further confirmation and gain an in-depth understanding on the butanethiol-induced doping of $MoTe_2$, XPS analysis was performed on an exfoliated $MoTe_2$ flake under three different conditions: pristine, annealed at 250 °C for 2 h in $N_2$ atmosphere, and thiol-treated. The scenarios are portrayed in Figure 2a−c, where black dotted circles denote Te vacancies in $MoTe_2$. In Figure 2c, the healed Te vacancies of the thiol-$MoTe_2$ are filled by red spheres, which represent the sulfur atoms of butanethiols. To monitor the amount of Te vacancies, we analyzed the shifts in the binding energy (BE) of Mo 3d and Te 3d. Toward this end, we have annealed the pristine $MoTe_2$ in $N_2$ by using a hot plate before thiol functionalization because it is reported that the Te vacancies can be introduced on $MoTe_2$ surface around 200 °C (UHV) or 250 °C ($N_2$) due to the weak Mo−Te bond strength.[33,34] Quantitative calculations to determine the number of Te vacancies generated by $N_2$ annealing are included in Figure S5.[35,36] As presented in blue in Figure 2d,e, the $N_2$ annealing resulted in a blue shift of ∼0.2 eV in both Mo 3d and Te 3d peaks compared to the pristine case (in black), indicative of the development of Te vacancies. In contrast, the thiol-$MoTe_2$ (in red), Mo 3d and Te 3d peaks exhibited a red shift of 0.15 and 0.3 eV, respectively, from the pristine condition, which implies that Te vacancies are healed by chemisorbed butanethiol on $MoTe_2$ surface. (Without $N_2$ annealing, butanethiol treatment on pristine $MoTe_2$ also leads to a red shift for both Mo and Te core-level spectra compared to the pristine case, Figure S6.) BE shifts in XPS spectra are commonly employed to identify the polarity changes of 2D TMD materials. These blue and red shifts align with previous results associated with electron and hole carrier doping effects on $MoTe_2$, respectively.[18,21] Besides, Figure S7 portrays the transfer characteristics of $MoTe_2$ FET under each condition (pristine, $N_2$-annealed, and after butanethiol treatment), along with the expected band diagrams. By and large, XPS analysis and electrical characteristics of thiol-$MoTe_2$ and its FET provide unambiguous evidence for the healing of Te vacancies with butanethiols, inducing efficient hole carrier doping in $MoTe_2$. High-resolution scanning transmission electron microscopy (HRSTEM) for both $N_2$-annealed $MoTe_2$ and thiol-$MoTe_2$ also proves that Te vacancies of $MoTe_2$ are effectively healed through the chemisorption of butanethiol. (See Figure S8 for details.)

Our p-doped thiol-$MoTe_2$ is exploited to realize the JFET devices, upon stacking n-$SnS_2$ on its surface, as depicted in the 3D schematic device view in Figure 3a. The electronic properties of $SnS_2$, especially its deep work function with high electron concentration, and excellent stability in ambient conditions make it highly suitable for air-stable practical electronic applications in conjunction with our thiol-$MoTe_2$.[28,37] The red spheres on the bottom of thiol-$MoTe_2$ portray sites, where the Te point vacancies are functionalized by the butanethiol. To form the van der Waals heterojunction, a $SnS_2$ flake has been precisely transferred on the top of the thiol-$MoTe_2$, followed by S/D electrode deposition processes for both $MoTe_2$ and $SnS_2$ flakes. The thiol treatment on $MoTe_2$ of the JFET was carried out on the entire $MoTe_2$ flake, including the area subsequently coated with Au S/D electrodes. Calculations of the Schottky barrier height, discussed in Figure S9, revealed no stark differences in the



https://doi.org/10.1021/acsnano.4c02207
*ACS Nano* 2024, 18, 18334−18343

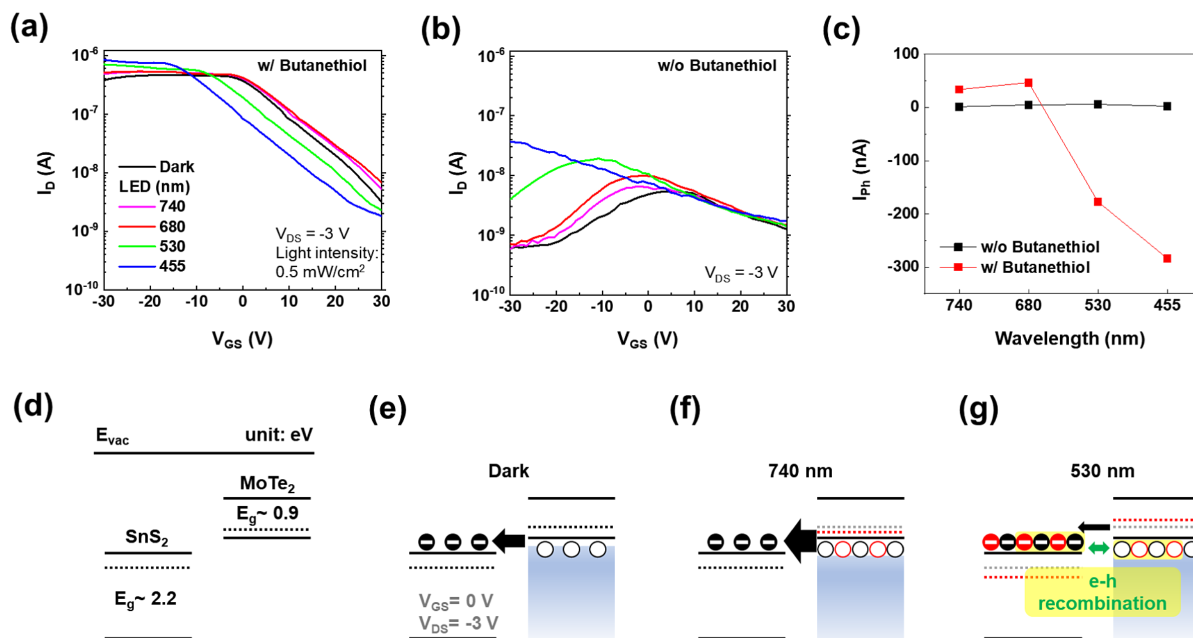


**Figure 4. Photoresponse properties and working mechanism of $SnS_2$/thiol-$MoTe_2$ JFET photodetector. (a) Transfer characteristics of the JFET photodetector showing normal PPR at 680 and 740 nm wavelengths, but unusual NPR at higher energy wavelengths 455 and 530 nm. (b) Transfer curves of control sample, whose photoresponse is very negligible at $V_{GS}$ = 0 V. (c) Photocurrent ($I_{Ph}$) as a function of incident wavelength at $V_{GS}$ = 0 V, exhibiting that a higher energy than 2.2 eV leads to NPR, only in case of the thiol-JFET. (d) Band diagrams of the two individual flakes before the junction formation. Schematic energy band of type III $SnS_2$/$MoTe_2$ heterojunction at $V_{GS}$ = 0 V and $V_{DS}$ = −3 V, explaining the PPR and NPR mechanisms: (e) dark, (f) 740 nm (PPR), and (g) 530 nm (NPR) illumination.**

results between with and without the presence of butanethiol under S/D electrodes. The details of device fabrications can be found in Methods section. Figure 3b shows the AFM topographical profiles of each flake integrated into the JFET device. The thicknesses of thiol-$MoTe_2$ and $SnS_2$ amounted to 9 and 27 nm, respectively. The semiconducting properties of two different 2H-phase TMDs have been revealed by Raman spectroscopy (Figure 3c).[26,27] The characteristic peaks of both materials have been observed in the $SnS_2$/thiol-$MoTe_2$ junction area. Interestingly, the intensity of the $SnS_2$ $A_{1g}$ peak in the $SnS_2$/thiol-$MoTe_2$ heterojunction decreased compared to the case of pristine $SnS_2$ due to either charge transfer or strong dipole−dipole coupling among the layers forming the van der Waals heterojunctions, indicating the existence of a strong interaction between $SnS_2$ and the underlying thiol-$MoTe_2$.[23,38] It is important to note that thiol-$MoTe_2$ and $SnS_2$ sheets interact in a van der Waals manner without losing their semiconducting properties, as previously observed from 2D van der Waals heterojunctions in the absence of chemical treatment.[23,26] Figure 3d illustrates the 2D cross-section of the interface between $SnS_2$ and thiol-$MoTe_2$, where our primary focuses lie on to explain antiambipolar transfer characteristics of the JFET. Under $V_{DS}$ = −1 V, the operation principle of the JFET can be categorized according to different $V_{GS}$ values: (i) $V_{GS}$ < 0 V, (ii) $V_{GS}$ = 0 V, and (iii) $V_{GS}$ > 0 V. In case (i), $SnS_2$ electrons are depleted, increasing the total resistance of the heterojunction channel, and accordingly perturbing the charge flow. Case iii exhibits high resistance, similarly to case (i), due to the hole depletion in thiol-$MoTe_2$. However, in case (ii), both $MoTe_2$ and $SnS_2$ channels have sufficient hole and electron carriers, thus the JFET can be expected to be in ON state. Based on this explanation, we could rationally expect that the overall transfer characteristics of $SnS_2$/thiol-$MoTe_2$ JFET should display antiambipolar behavior. Electrodes labeled 2 and 3 in Figure 3a were used for applying drain voltage and grounding, respectively, for all JFET measurements in this paper. Electrodes 1 and 2 were designed for thiol-$MoTe_2$ FET, while electrodes 3 and 4 were designed for $SnS_2$ FET. We found that our thiol-JFET displays antiambipolar transfer characteristics (red curve in Figure 3e) with $I_{ON}/I_{OFF}$ = $10^2$, which is comparable to previous reports.[28,39] The green transfer curve of the single-channel thiol-$MoTe_2$ FET in Figure 3e provides further confirmation of the effect of butanethiol surface treatment with a larger hole current than an electron current. The n-$SnS_2$ FET exhibits electron polarity with $I_{ON}/I_{OFF}$ = $10^7$. Significantly, all the electrical measurements of JFET, including the following photodetector applications, were carried out in ambient air thanks to the excellent air stability of both thiol-$MoTe_2$ and $SnS_2$.

As proof-of-concept applications, our $SnS_2$/thiol-$MoTe_2$ JFET has been integrated as a working phototransistor whose photoresponsive characteristics have undergone extensive examinations. The transfer characteristics of the phototransistor in Figure 4a reveal an expected positive photoresponse (PPR) when irradiated with 680 and 740 nm light. Additionally, unusual NPR (near $V_{GS}$ = 0 V) alongside PPR has been observed when using shorter wavelengths of 530 and 455 nm shone from a LED (0.5 mW $cm^{-2}$). This behavior indicates that two factors influence the photoresponse of our JFET: the LED wavelength and the $V_{GS}$. Prior to delving into the working mechanism of the intriguing NPR, we compared the photoresponse properties of $SnS_2$/thiol-$MoTe_2$ JFET with those of pristine $MoTe_2$. The latter displays the absence of perceivable NPR, and a minimal PPR effect (see Figure 4b,c). When plotting $I_{Ph}$ vs wavelength under $V_{GS}$ = 0 V in Figure 4c, where $I_{Ph}$ is defined as $I_{Ph} = I_{LED} - I_{Dark}$, it is evident that the device treated with butanethiol exhibits significantly higher $I_{Ph}$



https://doi.org/10.1021/acsnano.4c02207
ACS Nano 2024, 18, 18334−18343

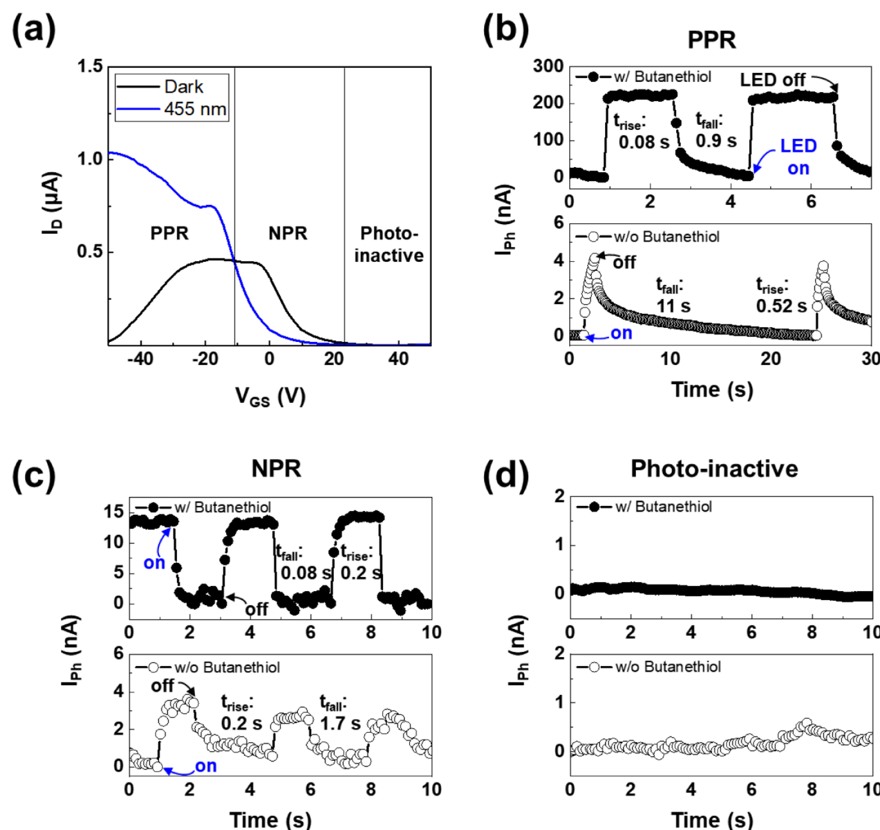


**Figure 5. Trimodal operation of $SnS_2$/thiol-$MoTe_2$ JFET photodetector.** (a) Transfer characteristics of JFET photodetector with PPR, NPR, and photoinactive mode depending on applied $V_{GS}$. (b−d) Time-resolved photoresponse of thiol-JFET and control sample under 455 nm LED illumination. For the photoactive PPR and NPR, −40 and 0 V of $V_{GS}$ are applied, respectively, while photoinactive mode is observed at $V_{GS}$ = 40 V.

values. This result confirms once again that our thiol-$MoTe_2$ improves the quality of the interface with $SnS_2$ by filling Te vacancies with butanethiol, thereby minimizing interface defects. (To understand the adverse effects of interface defects on the photoresponse property of JFET devices, a reversely stacked thiol-$MoTe_2$/$SnS_2$ is fabricated, and its photoresponse properties are shown in Figure S10.) In other words, Te point vacancy healing on $MoTe_2$ through thiol treatment can be used for forming various heterojunctions with different van der Waals materials. In Figure 4c, the transition of the photoresponse from PPR to NPR is evident as a function of wavelength. At $V_{GS}$ = 0 V, higher energy wavelengths (e.g., 455 and 530 nm) lead to NPR. However, NPR diminishes upon lowering the energy wavelengths (680 and 740 nm), which fail to excite photogenerated carriers in $SnS_2$. These observations underscore the importance of photoexcitation in $SnS_2$ for NPR, as lower energy photons tend to penetrate $SnS_2$ and excite only $MoTe_2$, leading to PPR. The band diagrams of $SnS_2$ and $MoTe_2$ should be taken into account, as both materials have different band gaps ($SnS_2$ ∼2.2 eV and $MoTe_2$ ∼0.9 eV).[23,40] Figure 4d illustrates the diagrams of $MoTe_2$ and $SnS_2$ before junction formation. The estimated work functions for $SnS_2$ and $MoTe_2$ amount to 5.2 and 4.9 eV, respectively, based on previous research.[6,26] According to Figure 4d, $MoTe_2$ and $SnS_2$ would form a type III junction, a prerequisite for BTBT tunneling.[41] After contact, electrons in $MoTe_2$ move into the $SnS_2$ side to establish charge equilibrium between the two TMDs in the dark condition. Both materials accumulate their majority carriers, as depicted in Figure 4e. Particularly, $V_{DS}$ = −3 V helps push up overall $MoTe_2$ bands, augmenting the BTBT tunneling possibilities of hole carriers from the valence band of $MoTe_2$ to the conduction band of $SnS_2$. Conversely, under the $V_{DS}$ > 0 V condition, we barely observed the NPR effect due to the inappropriate band alignment for BTBT. (See Figure S11 for details.) Therefore, reasonable explanations for the transition from PPR to NPR could be elucidated with the extent of electron−hole (e−h) recombination at the heterojunction between thiol-$MoTe_2$ and $SnS_2$. Upon exposure to the 740 nm LEDs (Figure 4f), only $MoTe_2$ got excited, yielding an accumulation of hole carriers in $MoTe_2$, which determines an increase of $I_D$. On the other hand, when both $SnS_2$ and $MoTe_2$ responded simultaneously to high energy photons, the electron concentration increased across the $SnS_2$ film, encompassing the heterojunction area where e−h recombination occurs. Especially, the number of excited electrons in $SnS_2$ exceeds the number of excited hole carriers in $MoTe_2$, given $SnS_2$'s superior photoresponse compared to $MoTe_2$, as demonstrated in Figure S12. As charge carriers depleted through e−h recombination (Figure 4g), the total $I_D$ of the JFET decreased, appearing as an abnormal NPR effect. The $SnS_2$/thiol-$MoTe_2$ JFET exhibited a *R* of 150 (PPR) and −50 (NPR) A $W^{-1}$ under the 455 nm LED, with a maximum detectivity (*D*) of 8 × $10^{11}$ and −1 × $10^{10}$ Jones. Compared with the control sample without thiol treatment, the *R* and *D* values of the $SnS_2$/thiol-$MoTe_2$ JFET are at least 20 times greater. Details for *R* and *D* calculations and plots for both devices are provided in Figure S13.


https://doi.org/10.1021/acsnano.4c02207
ACS Nano 2024, 18, 18334−18343

So far, our focus laid predominantly on $V_{GS}$ near 0 V to elucidate PPR and NPR of our JFET photodetector in response to incident photons' wavelengths. Very interestingly, we found that additional functionalities can be endowed upon $V_{GS}$ modulation. It can be clearly observed in Figures 4a and S11a, where a gradual decrease in absolute $I_{Ph}$ values is recorded until $V_{GS}$ reaches 40 V due to the decrease in hole concentration of $MoTe_2$ under positive $V_{GS}$. According to the transfer curves of thiol-JFET under dark conditions and the 455 nm LED in Figure 5a, there is photoinactive mode over 20 V of $V_{GS}$ as well as photoactive mode (PPR and NPR). Over 20 V of $V_{GS}$, the total $I_D$ of JFET mainly relied on the conductivity of $MoTe_2$, despite $SnS_2$ exhibiting a strong photoresponse under 455 nm LED. This photoinactive mode occurs when $MoTe_2$ hardly shows photoresponse in its OFF state, as shown in Figure S12. Conversely, the application of a negative $V_{GS}$ induced a photoresponse mainly driven by $SnS_2$ flakes, resulting in PPR. At $V_{GS}$ = 0 V, e−h recombination at the $MoTe_2$ and $SnS_2$ heterojunction with the BTBT effect leads to the previously discussed NPR effect. Considering another crucial parameter of the photodetector, we extracted and compared the photoswitching speeds of the thiol-treated JFET and control sample (Figure 5b−d). The PPR switching times at $V_{GS}$ = −40 V for the thiol-JFET were at least five times shorter than those for the control sample, with a rising time of 0.08 s and a falling time of 0.9 s compared to the control sample's 0.52 s rising time and 11 s falling time. At $V_{GS}$ = 0 V, while the control sample shows PPR, the thiol-JFET displayed NPR due to e−h recombination. This discrepancy arises from the control sample lacking a sufficient number of hole concentrations in $MoTe_2$ when $SnS_2$ generates excess photo-excited electrons. The limited number of hole carriers results in less efficient e−h recombination at the $SnS_2$/thiol-$MoTe_2$ interface, yet this is counterbalanced by the photogating effect in $MoTe_2$ inducing the PPR. However, the midgap defect states present in $MoTe_2$ of the control sample hinder the PPR effect,[42] leading to a relatively slower and smaller photocurrent response compared to NPR of the thiol-JEFT. In fact, a pivotal aspect of NPR lies in its notably quicker falling speed (0.08 s) compared to the rising speed (0.2 s), a characteristic not typically observed in conventional phototransistors due to charge trap/detrap in the defect states.[43−45] To demonstrate that our thiol-treated $MoTe_2$ and its device applications genuinely expand the utility of $MoTe_2$, Table S1 reports a detailed comparisons of NPR effects from various 2D heterostructures. Notably, demonstration of NPR, in particular based on a $MoTe_2$-based JFET, remains rare in the literature. Therefore, our thiol functionalization approach for $MoTe_2$ is very meaningful toward advanced optoelectronic applications.

## CONCLUSIONS

In summary, we have successfully achieved a reliable p-doping effect in $MoTe_2$ FETs through the grafting of thiol molecules at Te point vacancies. Upon butanethiol treatment, thiol-$MoTe_2$ FET demonstrated the 10-fold increase in maximum hole current, while maximum electron current decreased by 4 orders of magnitude compared to pristine $MoTe_2$ FET. Notably, our molecular engineering can be seamlessly integrated into van der Waals heterojunction systems, as exemplified by the $SnS_2$/thiol-$MoTe_2$ JFET, which exhibited intriguing antiambipolar transfer characteristics with an $I_{ON}/I_{OFF}$ ratio of $10^2$. Moreover, our JFET functioned as a photodetector, revealing a significant NPR ($R \sim -50$ A $W^{-1}$) attributed to BTBT, alongside normal PPR ($R \sim 150$ A $W^{-1}$) as a function of incident photons' wavelengths. NPR can be realized using a $MoTe_2$-based JFET, thanks to the enhanced hole polarities of thiol-$MoTe_2$. Beyond the superior optoelectronic properties demonstrated by our JFET, trimodal operation with PPR, NPR, and photoinactive mode was showcased through modulation of $V_{GS}$. These findings highlight the potential of molecular functionalization of $MoTe_2$ for developing reliable and high-performance p-$MoTe_2$ FETs and JFET photodetectors, which are poised to garner considerable attention in the field of 2D-based optoelectronics.

## METHODS

**Materials.** Bulk 2H-$MoTe_2$ and 2H-$SnS_2$ crystals were purchased from HQ graphene. CVD-grown monolayer $MoTe_2$ was purchased from 6Carbon Technology. 1-Butanethiol (product no. 112928) was purchased from Sigma-Aldrich.

**Device Fabrication and Functionalization.** *Single-Channel $MoTe_2$ FET.* $SiO_2$ (270 nm)/$n^+$-Si substrates were cleaned by acetone and ethanol in an ultrasonicator for 30 min each. $MoTe_2$ flakes were mechanically exfoliated from bulk crystals using polydimethylsiloxane (SYLGARDTM 184 Kit). Subsequently, we used another PDMS stamp, instead of scotch tape, to exfoliate a few layers thick $MoTe_2$ crystal from the original PDMS surface.[46] As on our PDMS stamp, we observed many isolated few layers thick $MoTe_2$ flakes, and we used an optical microscope to select the optimal one (based on the lateral size and uniformity) after covering with a glass slide the exfoliated $MoTe_2$ flakes supported on PDMS. (The thicknesses of all $MoTe_2$ flakes used in this study range from 5 to 10 nm.) Subsequently, S/D electrodes of Au/Cu (50/3 nm) were patterned by photolithography, thermal evaporation followed by a lift-off process. The as-prepared samples were mildly annealed at 150 °C for 2 h in a glovebox under $N_2$ atmosphere to improve the contacts and prevent additional Te defect formation. The substrates with pristine $MoTe_2$ FETs (multi-layer $MoTe_2$ flakes and CVD-grown $MoTe_2$ monolayer on as-grown sapphire glass in the case of XPS analysis) were fixed onto the lid of a 50 mL glass container containing 400 $\mu$L of 1-butanethiol. The $MoTe_2$ channel surfaces faced the liquid, and the containers were heated to saturate the butanethiol vapor at 70 °C for 3 h using a hot plate. Residual physiosorbed molecules were removed by postannealing the substrates at 70 °C for 1 h outside the glass container. All of the process was conducted inside the glovebox ($N_2$).

*$SnS_2$/$MoTe_2$ JFET.* Prior to S/D electrode deposition, the $SnS_2$ top layer was transferred onto thiol-$MoTe_2$ (pristine $MoTe_2$ for control sample) using the same mechanical exfoliation process to create a type III heterojunction. The alignment of the glass-supported $SnS_2$/PDMS sample on the thiol-$MoTe_2$/$SiO_2$/$n^+$-Si substrate has been accomplished using an optical microscope and CCD camera-equipped microaligner. Then, the aligned $SnS_2$ flake was transferred by imprinting onto $MoTe_2$/PDMS/glass toward the $SiO_2$ substrate by applying a vertical pressure. S/D electrodes of Au/Cu (50/3 nm) were then patterned as described earlier. The as-prepared JFET samples underwent the same mild annealing process at 150 °C for 2 h in the $N_2$ glovebox, in order to improve both contacts of $MoTe_2$ and $SnS_2$ at a same time.

**Optoelectronic Measurements.** Electrical measurements of single-channel devices were performed using a Keithley


https://doi.org/10.1021/acsnano.4c02207
ACS Nano 2024, 18, 18334−18343

dual-channel 2636A sourcemeter in a glovebox filled with $N_2$ under dark conditions. Photoresponse measurements of the phototransistor were carried out under 740, 680, 530, and 455 nm LEDs. The linear mobility $\mu_{Lin}$ was calculated by the following equation:

$$\mu_{Lin} = \frac{dI_D}{dV_{GS}} \times \frac{L}{WC_{ox}V_{DS}}$$

where $L$ and $W$ are the channel length and width, respectively, and $C_{ox}$ is the capacitance of the dielectric layer per unit area.

**Material Characterization.** Raman spectra were acquired in an air atmosphere using a 532 nm wavelength laser (Renishaw inVia spectrometer). All Raman spectra were calibrated using 520 $cm^{-1}$ of Si as a reference. XPS measurements were carried out with a basic chamber pressure of $\sim 10^{-9}$ mbar, and an Al anode as the X-ray source (X-ray radiation of 1486 eV)/spot sizes of 400 $\mu$m and pass energies of 200.00 eV for side energy scans and 10.00−20.00 eV for scans were used (Thermo Scientific K-Alpha). All XPS spectra were calibrated using the C 1s peak at 284.8 eV as a reference. For the AFM measurement, tapping mode atomic force microscopy imaging was executed in air (Bruker Dimension Icon). The tip model is TESPA-V2, and the tip stiffness K is 42 N $m^{-1}$. High-resolution scanning transmission electron microscopy images were obtained using an aberration-corrected Thermo Fisher Scientific Titan microscope operated at 200 kV. Images were acquired with a 30 pA beam current and postprocessed using deep convolutional neural networks.[47]

## ASSOCIATED CONTENT

### Supporting Information

The Supporting Information is available free of charge at https://pubs.acs.org/doi/10.1021/acsnano.4c02207.

Optical microscopy images and corresponding AFM line profiles of pristine and thiol-treated multilayer $MoTe_2$ flakes; AFM topographical imaging of $MoTe_2$ and thiol-$MoTe_2$ surfaces; transfer characteristics and corresponding mobility plots of $MoTe_2$ FET before and after butanethiol treatment; transfer and output characteristics of pristine and thiol-$MoTe_2$ FET under different ambient conditions ($N_2$, air, and UHV $\sim 10^{-5}$ Torr); evolution of the XPS spectra of CVD-grown monolayer $MoTe_2$ on sapphire glass with high temperature hot plate annealing under $N_2$; high-resolution XPS analysis of surface-functionalized $MoTe_2$; transfer characteristics and corresponding band diagrams under three different conditions (pristine, $N_2$-annealed, and after butanethiol treatment); high-resolution STEM images and related histograms of Mo−Mo distance for annealed $MoTe_2$ and thiol-$MoTe_2$; transfer characteristics at low temperature and Schottky barrier height calculation of pristine and thiol-$MoTe_2$ FET; photoresponse of the reversely stacked thiol-$MoTe_2$/$SnS_2$ JFET; photoresponse of the thiol-JFET under $V_{DS} = -3$ V and $V_{DS} = 3$ V, along with expected band diagrams; photoresponse of single-channel FETs; schematic cross section and calculation details for responsivity and detectivity; reported performance of NPR devices depending on type of van der Waals heterojunction (PDF)

## AUTHOR INFORMATION


### Corresponding Author

**Paolo Samorì** − *University of Strasbourg, CNRS, Institut de Science et d'Ingénierie Supramoléculaires, Strasbourg 67000, France*; orcid.org/0000-0001-6256-8281; Email: samori@unistra.fr

### Authors

**Yeonsu Jeong** − *University of Strasbourg, CNRS, Institut de Science et d'Ingénierie Supramoléculaires, Strasbourg 67000, France*; orcid.org/0000-0001-6233-6640

**Bin Han** − *University of Strasbourg, CNRS, Institut de Science et d'Ingénierie Supramoléculaires, Strasbourg 67000, France*

**Adrián Tamayo** − *University of Strasbourg, CNRS, Institut de Science et d'Ingénierie Supramoléculaires, Strasbourg 67000, France*

**Nathalie Claes** − *Electron Microscopy for Materials Science (EMAT) and NANOlab Center of Excellence, University of Antwerp, Antwerp 2020, Belgium*

**Sara Bals** − *Electron Microscopy for Materials Science (EMAT) and NANOlab Center of Excellence, University of Antwerp, Antwerp 2020, Belgium*; orcid.org/0000-0002-4249-8017

Complete contact information is available at: https://pubs.acs.org/10.1021/acsnano.4c02207


### Author Contributions

Y.J. and P.S. conceived the experiments and designed the study. Y.J. performed all optoelectrical and material characterization. B.H. performed the XPS measurement. A.T. performed AFM measurement and analyzed electrical performance of the devices. N.C. and S.B conducted HRSTEM measurements and analyses. All authors discussed the results and contributed to the interpretation of data. Y.J. and P.S. cowrote the paper with input from all coauthors.

### Notes

The authors declare no competing financial interest.

## ACKNOWLEDGMENTS


The authors acknowledge the financial support from the FLAG-ERA project MULTISPIN funded by the Agence Nationale de la Recherche (ANR-21-GRF1-0003-01). We also acknowledge funding from the European Union's Horizon Europe research and innovation programme through the project HYPERSONIC (GA-101129613) and the ERC project SUPRA2DMAT (GA-833707) as well as the ANR through the Interdisciplinary Thematic Institute SysChem via the IdEx Unistra (ANR-10-IDEX-0002) within the program Investissement d'Avenir, the Foundation Jean-Marie Lehn and the Institut Universitaire de France (IUF). This work was also supported by National Research Foundation of Korea (NRF) grant funded by Korea government (MSIT) (No. RS-2023-00251360).


## REFERENCES


(1) Radisavljevic, B.; Radenovic, A.; Brivio, J.; Giacometti, V.; Kis, A. Single-Layer $MoS_2$ Transistors. *Nat. Nanotechnol.* **2011**, *6*, 147−150.

(2) Zhao, Y.; Gali, S. M.; Wang, C.; Pershin, A.; Slassi, A.; Beljonne, D.; Samorì, P. Molecular Functionalization of Chemically Active Defects in $WSe_2$ for Enhanced Opto-Electronics. *Adv. Funct. Mater.* **2020**, *30*, 2005045.

(3) Zhou, X.; Hu, X.; Yu, J.; Liu, S.; Shu, Z.; Zhang, Q.; Li, H.; Ma, Y.; Xu, H.; Zhai, T. 2D Layered Material-Based van der Waals

Heterostructures for Optoelectronics. *Adv. Funct. Mater.* **2018**, *28*, 1706587.
(4) Cheon, Y.; Lim, S. Y.; Kim, K.; Cheong, H. Structural Phase Transition and Interlayer Coupling in Few-Layer 1T′and $T_d$ $MoTe_2$. *ACS Nano* **2021**, *15*, 2962−2970.
(5) Ruppert, C.; Aslan, B.; Heinz, T. F. Optical Properties and Band Gap of Single- and Few-Layer $MoTe_2$ Crystals. *Nano Lett.* **2014**, *14*, 6231−6236.
(6) Ahn, J.; Kyhm, J.; Kang, H. K.; Kwon, N.; Kim, H.; Park, S.; Hwang, D. K. 2D $MoTe_2$/$ReS_2$ van der Waals Heterostructure for High-Performance and Linear Polarization-Sensitive Photodetector. *ACS Photonics* **2021**, *8*, 2650−2658.
(7) Cai, J.; Sun, Z.; Wu, P.; Tripathi, R.; Lan, H.-Y.; Kong, J.; Chen, Z.; Appenzeller, J. High-Performance Complementary Circuits from Two-Dimensional $MoTe_2$. *Nano Lett.* **2023**, *23*, 10939−10945.
(8) Cho, Y.; Park, J. H.; Kim, M.; Jeong, Y.; Ahn, J.; Kim, T.; Choi, H.; Yi, Y.; Im, S. Fully Transparent p-$MoTe_2$ 2D Transistors Using Ultrathin MoOx/Pt Contact Media for Indium-Tin-Oxide Source/Drain. *Adv. Funct. Mater.* **2018**, *28*, 1801204.
(9) Pradhan, N. R.; Rhodes, D.; Feng, S.; Xin, Y.; Memaran, S.; Moon, B.-H.; Terrones, H.; Terrones, M.; Balicas, L. Field-Effect Transistors Based on Few-Layered $\alpha$-$MoTe_2$. *ACS Nano* **2014**, *8*, 5911−5920.
(10) Park, Y. J.; Katiyar, A. K.; Hoang, A. T.; Ahn, J. H. Controllable p- and n-Type Conversion of $MoTe_2$ via Oxide Interfacial Layer for Logic Circuits. *Small* **2019**, *15*, 1901772.
(11) Townsend, N. J.; Amit, I.; Craciun, M. F.; Russo, S. Sub 20 meV Schottky Barriers in Metal/$MoTe_2$ Junctions. *2D Mater.* **2018**, *5*, 025023.
(12) Lin, Y. F.; Xu, Y.; Wang, S. T.; Li, S. L.; Yamamoto, M.; Aparecido-Ferreira, A.; Li, W.; Sun, H.; Nakaharai, S.; Jian, W. B.; et al. Ambipolar $MoTe_2$ Transistors and Their Applications in Logic Circuits. *Adv. Mater.* **2014**, *26*, 3263−3269.
(13) Liu, X.; Qu, D.; Wang, L.; Huang, M.; Yuan, Y.; Chen, P.; Qu, Y.; Sun, J.; Yoo, W. J. Charge Density Depinning in Defective $MoTe_2$ Transistor by Oxygen Intercalation. *Adv. Funct. Mater.* **2020**, *30*, 2004880.
(14) Elibol, K.; Susi, T.; Argentero, G.; Ahmadpour Monazam, M. R.; Pennycook, T. J.; Meyer, J. C.; Kotakoski, J. Atomic Structure of Intrinsic and Electron-Irradiation-Induced Defects in $MoTe_2$. *Chem. Mater.* **2018**, *30*, 1230−1238.
(15) Haldar, S.; Vovusha, H.; Yadav, M. K.; Eriksson, O.; Sanyal, B. Systematic Study of Structural, Electronic, and Optical Properties of Atomic-Scale Defects in the Two-Dimensional Transition Metal Dichalcogenides $MX_2$ (M = Mo, W; X = S, Se, Te). *Phys. Rev. B* **2015**, *92*, 235408.
(16) Chang, Y. M.; Yang, S. H.; Lin, C. Y.; Chen, C. H.; Lien, C. H.; Jian, W. B.; Ueno, K.; Suen, Y. W.; Tsukagoshi, K.; Lin, Y. F. Reversible and Precisely Controllable p/n-Type Doping of $MoTe_2$ Transistors through Electrothermal Doping. *Adv. Mater.* **2018**, *30*, 1706995.
(17) Ke, Y.; Song, X.; Qi, D.; Liu, J.; Hao, Q.; Wang, Z.; Tang, S.; Zhang, W. Modulation of Electrical Properties with Controllable Local Doping in Multilayer $MoTe_2$ Transistors. *Adv. Electron. Mater.* **2020**, *6*, 2000532.
(18) Qu, D.; Liu, X.; Huang, M.; Lee, C.; Ahmed, F.; Kim, H.; Ruoff, R. S.; Hone, J.; Yoo, W. J. Carrier-Type Modulation and Mobility Improvement of Thin $MoTe_2$. *Adv. Mater.* **2017**, *29*, 1606433.
(19) Cho, Y.; Lee, S.; Cho, H.; Kang, D.; Yi, Y.; Kim, K.; Park, J. H.; Im, S. Damage-Free Charge Transfer Doping of 2D Transition Metal Dichalcogenide Channels by van der Waals Stamping of $MoO_3$ and LiF. *Small Methods* **2022**, *6*, 2101073.
(20) Nguyen, P. H.; Nguyen, D. H.; Kim, H.; Jeong, H. M.; Oh, H. M.; Jeong, M. S. Synergistic hole-doping on ultrathin $MoTe_2$ for highly stable unipolar field-effect transistor. *Appl. Surf. Sci.* **2022**, *596*, 153567.
(21) Lee, D. H.; Rabeel, M.; Han, Y.; Kim, H.; Khan, M. F.; Kim, D.-K.; Yoo, H. Self-Assembled Monolayer Doping for $MoTe_2$ Field-Effect Transistors: Overcoming PN Doping Challenges in Transition Metal Dichalcogenides. *ACS Appl. Mater. Interfaces* **2023**, *15*, 51518−51526.
(22) Ippolito, S.; Samorì, P. Defect Engineering Strategies Toward Controlled Functionalization of Solution-Processed Transition Metal Dichalcogenides. *Small Sci.* **2022**, *2*, 2100122.
(23) Jeong, Y.; Kim, T.; Cho, H.; Ahn, J.; Hong, S.; Hwang, D. K.; Im, S. Negative Photoresponse Switching via Electron−Hole Recombination at The Type III Junction of $MoTe_2$ Channel/$SnS_2$ Top Layer. *Adv. Mater.* **2023**, *35*, 2304599.
(24) Szabo, A.; Koester, S. J.; Luisier, M. Ab-Initio Simulation of van der Waals $MoTe_2$−$SnS_2$ Heterotunneling FETs for Low-Power Electronics. *IEEE Electron Device Lett.* **2015**, *36*, 514−516.
(25) Yang, T.; Zheng, B.; Wang, Z.; Xu, T.; Pan, C.; Zou, J.; Zhang, X.; Qi, Z.; Liu, H.; Feng, Y.; Hu, W.; Miao, F.; Sun, L.; Duan, X.; Pan, A. Van der Waals Epitaxial Growth and Optoelectronics of Large-Scale $WSe_2$/$SnS_2$ Vertical Bilayer p−n Junctions. *Nat. Commun.* **2017**, *8*, 1906.
(26) Zhou, X.; Hu, X.; Zhou, S.; Song, H.; Zhang, Q.; Pi, L.; Li, L.; Li, H.; Lü, J.; Zhai, T. Tunneling Diode Based on $WSe_2$/$SnS_2$ Heterostructure Incorporating High Detectivity and Responsivity. *Adv. Mater.* **2018**, *30*, 1703286.
(27) Kim, S.; Du, H.; Kim, T.; Shin, S.; Song, H.-K.; Kim, H.; Kang, D.; Lee, C.-W.; Seo, S. Gate-Switchable Rectification in Isotype van der Waals Heterostructure of Multilayer $MoTe_2$/$SnS_2$ with Large Band Offsets. *Npj 2D Mater. Appl.* **2020**, *4*, 15.
(28) Chen, C. F.; Yang, S. H.; Lin, C. Y.; Lee, M. P.; Tsai, M. Y.; Yang, F. S.; Chang, Y. M.; Li, M.; Lee, K. C.; Ueno, K.; Shi, Y.; Lien, C.-H.; Wu, W.-W.; Chiu, P.-W.; Li, W.; Lo, S.-T.; Lin, Y.-F. Reversible Charge-Polarity Control for Multioperation-Mode Transistors Based on van der Waals Heterostructures. *Adv. Sci.* **2022**, *9*, 2106016.
(29) Rani, A.; DiCamillo, K.; Khan, M. A. H.; Paranjape, M.; Zaghloul, M. E. Tuning the Polarity of $MoTe_2$ FETs by Varying the Channel Thickness for Gas-Sensing Applications. *Sensors* **2019**, *19*, 2551.
(30) Ghosh, S.; Varghese, A.; Jawa, H.; Yin, Y.; Medhekar, N. V.; Lodha, S. Polarity-Tunable Photocurrent through Band Alignment Engineering in a High-Speed $WSe_2$/$SnSe_2$ Diode with Large Negative Responsivity. *ACS Nano* **2022**, *16*, 4578−4587.
(31) Tan, C.; Yin, S.; Chen, J.; Lu, Y.; Wei, W.; Du, H.; Liu, K.; Wang, F.; Zhai, T.; Li, L. Broken-Gap $PtS_2$/$WSe_2$ van der Waals Heterojunction with Ultrahigh Reverse Rectification and Fast Photoresponse. *ACS Nano* **2021**, *15*, 8328−8337.
(32) Schwarz, A.; Alon-Yehezkel, H.; Levi, A.; Yadav, R. K.; Majhi, K.; Tzuriel, Y.; Hoang, L.; Bailey, C. S.; Brumme, T.; Mannix, A. J.; Cohen, H.; Yalon, E.; Heine, T.; Pop, E.; Cheshnovsky, O.; Naveh, D. Thiol-Based Defect Healing of $WSe_2$ and $WS_2$. *Npj 2D Mater. Appl.* **2023**, *7*, 59.
(33) Zhu, H.; Wang, Q.; Cheng, L.; Addou, R.; Kim, J.; Kim, M. J.; Wallace, R. M. Defects and Surface Structural Stability of $MoTe_2$ under Vacuum Annealing. *ACS Nano* **2017**, *11*, 11005−11014.
(34) Ahmed, F.; Shafi, A. M.; Mackenzie, D. M. A.; Qureshi, M. A.; Fernandez, H. A.; Yoon, H. H.; Uddin, M. G.; Kuittinen, M.; Sun, Z.; Lipsanen, H. Multilayer $MoTe_2$ Field-Effect Transistor at High Temperatures. *Adv. Mater. Interfaces* **2021**, *8* (22), 2100950.
(35) Bertolazzi, S.; Bonacchi, S.; Nan, G.; Pershin, A.; Beljonne, D.; Samorì, P. Engineering Chemically Active Defects in Monolayer $MoS_2$ Transistors via Ion-Beam Irradiation and Their Healing via Vapor Deposition of Alkanethiols. *Adv. Mater.* **2017**, *29*, 1606760.
(36) Han, B.; Gali, S. M.; Dai, S.; Beljonne, D.; Samorì, P. Isomer Discrimination via Defect Engineering in Monolayer $MoS_2$. *ACS Nano* **2023**, *17*, 17956−17965.
(37) Zhou, X.; Zhang, Q.; Gan, L.; Li, H.; Zhai, T. Large-Size Growth of Ultrathin $SnS_2$ Nanosheets and High Performance for Phototransistors. *Adv. Funct. Mater.* **2016**, *26*, 4405−4413.
(38) Natarajan, V.; Ahmad, M.; Sharma, J. P.; Sathya, A.; Sharma, P. K.; Thangaraj, R. Interfacial Charge-Transfer for Robust Raman Quenching in Staggered Band Aligned n-$SnS_2$/p-rGO Heterostructures. *Appl. Surf. Sci.* **2021**, *550*, 149356.


https://doi.org/10.1021/acsnano.4c02207
*ACS Nano* 2024, 18, 18334−18343

(39) Li, Y.; Wang, Y.; Huang, L.; Wang, X.; Li, X.; Deng, H.-X.; Wei, Z.; Li, J. Anti-Ambipolar Field-Effect Transistors Based on Few-Layer 2D Transition Metal Dichalcogenides. *ACS Appl. Mater. Interfaces* **2016**, *8*, 15574−15581.
(40) Kang, J.; Tongay, S.; Zhou, J.; Li, J.; Wu, J. Band Offsets and Heterostructures of Two-Dimensional Semiconductors. *Appl. Phys. Lett.* **2013**, *102*, 012111.
(41) Rajbanshi, B.; Sarkar, S.; Sarkar, P. The Electronic and Optical Properties of $MoS_{2(1-x)}Se_{2x}$ and $MoS_{2(1-x)}Te_{2x}$ Monolayers. *Phys. Chem. Chem. Phys.* **2015**, *17*, 26166.
(42) Ghimire, M. K.; Ji, H.; Gul, H. Z.; Yi, H.; Jiang, J.; Lim, S. C. Defect-Affected Photocurrent in $MoTe_2$ FETs. *ACS Appl. Mater. Interfaces* **2019**, *11*, 10068−10073.
(43) Zhao, Y.; Bertolazzi, S.; Samorì, P. A Universal Approach toward Light-Responsive Two-Dimensional Electronics: Chemically Tailored Hybrid van der Waals Heterostructures. *ACS Nano* **2019**, *13*, 4814−4825.
(44) Zhou, J.; Li, H.; Tian, M.; Chen, A.; Chen, L.; Pu, D.; Hu, J.; Cao, J.; Li, L.; Xu, X.; et al. Multi-Stimuli-Responsive Synapse Based on Vertical van der Waals Heterostructures. *ACS Appl. Mater. Interfaces* **2022**, *14*, 35917−35926.
(45) Wang, H.; Wang, X.; Chen, Y.; Zhang, S.; Jiang, W.; Zhang, X.; Qin, J.; Wang, J.; Li, X.; Pan, Y.; et al. Extremely Low Dark Current $MoS_2$ Photodetector via 2D Halide Perovskite as the Electron Reservoir. *Adv. Optic. Mater.* **2020**, *8*, 1901402.
(46) Choi, K.; Lee, Y. T.; Min, S.-W.; Lee, H. S.; Nam, T.; Kim, H.; Im, S. Direct Imprinting of $MoS_2$ Flakes on a Patterned Gate for Nanosheet Transistors. *J. Mater. Chem. C* **2013**, *1*, 7803−7807.
(47) Lobato, I.; Friedrich, T.; Aert, S. V. Deep Convolutional Neural Networks to Restore Single-Shot Electron Microscopy Images. *Npj Comput. Mater.* **2024**, *10*, 10.



https://doi.org/10.1021/acsnano.4c02207
*ACS Nano* 2024, 18, 18334−18343